Accepted Manuscript

Title: X-Ray tomography of additive-manufactured zirconia: processing defects – strength relations

Authors: M. Saâdaoui, F. Khaldoun, J. Adrien, H. Reveron, J. Chevalier

PII: S0955-2219(19)30234-1
DOI: https://doi.org/10.1016/j.jeurceramsoc.2019.04.010
Reference: JECS 12441

To appear in: *Journal of the European Ceramic Society*

Received date: 11 March 2019
Revised date: 4 April 2019
Accepted date: 5 April 2019

Please cite this article as: Saâdaoui M, Khaldoun F, Adrien J, Reveron H, Chevalier J, X-Ray tomography of additive-manufactured zirconia: processing defects – strength relations, *Journal of the European Ceramic Society* (2019), https://doi.org/10.1016/j.jeurceramsoc.2019.04.010

X-Ray tomography of additive-manufactured zirconia: processing defects – strength relations

M. Saâdaoui[1], F. Khaldoun[1], J. Adrien[2], H. Reveron[2], J. Chevalier[2]

[1]Université Mohamed V de Rabat, EMI, LERSIM, Avenue Ibn Sina, 10000 Rabat, Morocco

[2]Université de Lyon, INSA de Lyon, MATEIS CNRS UMR5510, 20 Avenue Albert Einstein, F-69621 Villeurbanne Cedex, France

Abstract

X-ray Computed Tomography (XCT) analysis was applied to identify and quantify typical defects in dense 3Y-TZP zirconia processed by the Lithography-based Ceramic Manufacturing (LCM) technique. XCT derived strengths were anticipated from the XCT data and compared to experimental measurement. A good agreement between XCT data, bending strength measurement and fractographic analysis demonstrates the suitability of X-ray tomography for both defects detection and predictive mechanical strength estimation. It allows also to rank the different defects related to LCM in terms of their criticality versus mechanical resistance.

Key words: X-ray computed tomography, additive manufacturing, defects, strength, zirconia.

1. Introduction

Additive manufacturing (AM) is a process which enables to produce an object by adding material layer-by-layer from a 3D model data. This technology is currently developed for ceramic materials to avoid expensive machining, to obtain complex shapes or even to process geometries that could not be produced by other technologies [1, 2]. Different AM techniques have been used for these materials, among which are Direct Ink-jet Printing (DIP) [3], robocasting or direct ink writing (DIW) [1], Selective Laser Melting (SLM) [4], Selective Laser Sintering (SLS) [5,6], Stereolithography (SLA for StereoLithography Apparatus) [7], Lithography-based Ceramic Manufacturing (LCM) [8] and Ceramic On-Demand Extrusion (CODE) [9]. Most research and developments in AM of ceramic materials are related to

alumina and zirconia based ceramics for which high densities and promising mechanical properties, sometimes comparable to those of conventional manufacturing, could be reached (Table 1). However, it is still premature to make a direct comparison of the different processes due to insufficient data and to the non uniformity of the mechanical testing methods used to evaluate the final products. Moreover, the strength reliability of AM ceramics is still a challenge that requires to clarify the interdependencies between their final properties and the processes. In particular, only few works have been devoted to the characterization of the defects inherent to AM, which is crucial for the optimization of the mechanical properties. For example, Hagedorn et al. [28] reported that SLM of a zirconia toughened alumina (ZTA) ceramic resulted in crack formation that could be avoided by high-temperature preheating below the melting point of the material. In the case of stereolithography manufacturing of alumina, it has been shown [29] that large cracks and delamination between layers could be suppressed using an optimized two-step debinding process. Harrer et al. [20] have shown that for Y-TZP zirconia manufactured using the LCM technology, defects could be induced at different steps of the process, especially during the detachment of the green body from the building platform. The authors proposed some improvements of the manufacturing process to reduce the defects and their influence on the strength, which depend on the layers architecture and the loading configuration. Gan and Wong [30] have reported that the printing defects and the flexural strength of SLM manufactured alumina composites depend on the layer thickness, which shows that internal defects between layers may also compromise strength.

Microstructural characterization of ceramic materials is commonly achieved using optical or Scanning Electron Microscopy (SEM) that provides only 2D information of outer surfaces. Successive sectioning and subsequent microscopy are thus needed to evaluate 3D microstructure. X-ray Computed Tomography (XCT) is a non-destructive technique that receives increasing attention as it enables new insight into 3D microstructure [31,32]. It is based on X-ray attenuation and 3D reconstruction of the internal structure from sequential 2D projection images, with a typical resolution of few microns. Particular interest has been recently shown for the application of XCT in the field of AM, to evaluate AM methods, to control the geometry of the produced components or to characterize their microstructure [33-37]. In the field of ceramic materials, XCT have been particularly used for structural or damage characterization of ceramic matrix composites [38-43] and to evaluate pore morphology and interconnectivity of porous or cellular ceramics [44-50]. XCT analysis was also applied to follow the microstructural evolutions during the compaction process of

ceramic materials [51] or their sintering [52-54], and to investigate indentation induced cracking in dense alumina [55]. Pecanac et al. [56] used computed tomography data for numerical simulation of the mechanical behavior and strength prediction of tubular porous ceramics containing large defects. However, to our knowledge, this method has not been systematically applied to identify critical flaws in dense ceramics and their correlation to the mechanical properties. This study thus focuses on the application of XCT to characterize typical defects induced in a tetragonal polycrystalline zirconia stabilized with 3 mol % of yttria (3Y-TZP) processed by the LCM technology and to investigate their correlation with the bending strength.

2. Material and Methods

2.1. Material and samples

In this work, samples of tetragonal polycrystalline zirconia (3Y-TZP), received as rectangular bars (2.2 x 2.5 x 25 mm^3), were produced by Lithoz Gmbh (Austria). The materials were manufactured using the technique of Lithography-based Ceramic Manufacturing (LCM), the principle of which is based on a selective polymerization of a photosensitive ceramic source material obtained by dispersing a ceramic powder into a mixture of photocurable monomers. A laser beam is deflected onto the positions calculated by the CAD software and hardens or polymerizes the binder, so that the desired object is built up layer-by- layer. The material was identical to that described in [20]. In summary, the slurries were composed of 42 vol.% of 3Y-TZP ceramic powder and a photopolymerizable monomer mixture based on acrylates and methacrylates. Green bodies were first printed with a layer thickness of 25 µm, then they were cleaned and debinded under air atmosphere to remove the organic photopolymer matrix, before sintering at 1450°C for 2 hours. Two different layer architectures were produced by upright (U) or horizontal (H) building (fig. 1). Both materials were highly dense (relative density of 99%) and characterized by identical elastic properties. The Young's modulus and Poisson's ratio determined by the resonance vibration method were of 213 GPa and 0.3 respectively, and the Vickers hardness was of 13.1 GPa. The final microstructure (Fig. 2) was isotropic for both architectures with identical mean fine grain size of 0.5 ± 0.2µm (evaluated by the linear-intercept method over 200 grains and applying a factor of 1.56 to account for the 2D to 3D correction), which is typical of conventionally manufactured 3Y-TZP [57].

2.2. X-ray computed tomography

Systematic XCT analysis was carried out before fracture on most samples (21 from a total of 26 for each architecture), to identify typical LCM defects and quantify their size / distribution. XCT measurements were carried out using a Phoenix vTomeX/CT scanner (GE Phoenix | X-Ray GmbH, Germany). A continuous rotation was used and the integration time was 1000 ms for each of the 900 projections acquired over 360°. These parameters resulted in measurement periods of 15 minutes for a complete scan. The experiments were performed at a voltage of 140 kV and a current of 80 μA with a copper filter of 0.3 mm on the X-ray tube. XCT scans were generated in 4 identical steps, over a total length of 10 mm (in z direction) at the center of the samples. Each scan step allowed to obtain a stack of 1250 slices, perpendicular or parallel to the layers respectively in H and U samples (Fig. 1), with a voxel size of 2 μm. The cone-beam XCT data were reconstructed by a filtered back projection Feldkamp-algorithm. The reconstructed data were processed and visualized with the public domain ImageJ/Fiji shareware. In order to allow quantitative analysis of defects distributions and correlation with SEM micrographs, a low scan speed was achieved with improved conditions i.e., 900 projections and averaging 3 images at each step angle for selected samples to improve the quality (i.e. signal/noise ratio) of XCT images.

2.3. Strength measurements

To characterize the ‘as received’ surface state, the samples were only chamfered on the tensile side and they were tested so as the fracture plane was parallel or perpendicular to the layers respectively for U and H samples (Fig. 1). Due to a slight curvature of the samples, three points bending configuration was chosen rather than the generally more suitable 4 points one (where the stress is constant between the inner spans), to ovoid asymmetrical bending which would result finally in a more complex stress distribution. The three-points bending were performed on 26 samples of each architecture, with a span of 20 mm and a cross-head speed of 2 mm/min, using a universal hydraulic INSTRON 8500 testing machine.

3. Results and discussion

3.1. Defects characterization by XCT

Typical cross-sectional XCT-images of H and U samples are shown in Fig. 3. They allowed to identify four types of defects, already observed by fractography in LCM processed Y-TZP with architectures similar to those used in the present study [20]: large surface defects, pores, delamination's and agglomerates. In addition to these defects, cracks (marked with the letter C in Fig. 3), were also identified in U samples.

Large surface defects and delamination's, examples of which can be seen in Fig. 3, are typical of H samples and result from the removing of the specimens from the building platform. Indeed, the primary layer (in contact with the platform) that ensures the adherence of the sample on the building platform in the LCM process [20] has not been removed for this study. Surface defects can be distinguished by their irregular shape and delamination's by their elongated shape at the edges.

Pores were easily detected by XCT analysis as they provide sufficient X-Ray absorption contrast (Fig. 3). From 3D reconstructions (Fig. 4), it can be seen that they are mostly spherical for both architectures and are distributed throughout the entire scanned volume of U samples. By contrast, for H samples, the pores are often concentrated near the largest surface and within a central channel perpendicular to the layers. Fig. 5 shows typical differential and cumulative size distributions (in number) of pores, determined automatically using imageJ software, within the total scanned volume (length of 10 mm at the centre of samples). Given the thresholding used to remove background noise, only pores with equivalent sphere diameters (ESD) larger than 7 µm were detected. Reproducible and similar positively skewed distributions were observed for both architectures and the range of 7 to 20 µm is the dominant pore size for both architectures, with cumulative frequency exceeding 90%. The average pore size based on the value of D_{50} was determined from the cumulative pore size distribution of Fig. 5b and both architectures presented a similar value of 11 µm. The maximum of the distribution is at an ESD in the range of 8 - 10 µm and two other peaks can be seen at about 15 and 20 µm, with a lower number of pores. The largest ESD observed in the scanned zone was of 54 µm, detected in H sample. The sphericity was also determined and it was close to 1 for 90% of pores, confirming that they have a quite perfect spherical shape.

Agglomerates could be a consequence of the powder-binder preparation process and correspond to large under-densified zones. This differential densification didn't always provide sufficient X-Ray absorption contrast necessary to detect these defects by XCT analysis. They could be detected only by scrolling through the slice projections of U samples

(Fig. 3), due to the presence of characteristic surrounding small voids that provide higher contrast. 3D reconstruction (Fig. 6) showed that they are in the form of circular discs parallel to the layers, with an average thickness of 22 µm, which is on the order of the layers thickness. The agglomerates size distribution (Fig. 7) was determined manually as the X-Ray absorption contrast was not sufficient for automated detection of these defects. It is shown that agglomerate diameters lay in the range of 20-180 µm with a maximum frequency at 50 µm. Most of them are smaller than 100 µm with cumulative frequency of 94%. The average agglomerate size based on the value of D_{50} was of 56 µm.

Cracks emanating from agglomerates (marked with the letter C in Fig. 3) were often detected in U samples. They extend perpendicularly to the cross section of the agglomerates, over a width equivalent to the thickness of the latter's. Due to this orientation (parallel to the stress direction for U sample), these cracks would not be relevant to fracture initiation in the used loading configuration.

3.2. Flexural strength

Fig. 8 shows a Weibull plot of the strength data for U and H architectures. Unbiased values of the Weibull modulus, m, and the characteristic strength σ_0 (the stress corresponding to 63% fracture probability), with their 90% confidence intervals, were calculated following [58]. The obtained values of m were 11.2 [7.9-15] for U samples and 6.4 [4.5-8.6] for H samples and σ_0 was of 939 [810-968] MPa and 851[825-877] MPa respectively for U and H samples. The results are in accordance with those of four points bending tests in [20], with a lower difference between the strengths of H and U samples in the present work.

3.3. XCT derived critical defects

3.3.1. Detection and classification

A systematic examination of the XCT scans performed before fracture was performed to identify the potential fracture initiating defects. The investigation was started from the tensile side and two H samples fractured out of the scanned zone were eliminated. For each sample, four potential critical defects were detected (one in each of the 4 scanned volumes) then their sizes, a_{CT}, and their locations along the longitudinal direction (z axe in Fig. 1), z_{CT}, were measured from the sample center. Considering a fixed applied load, the stress intensity factor corresponding to each defect was determined taking into account the linear decrease of the

stress from its maximal value, σ_{max} (reached at the centre of the tensile side, in the used 3 point bending configuration):

$$K_I = \sigma_{max}\left(\frac{1-Z_{CT}}{10}\right)Y\sqrt{a_{CT}} \qquad (1)$$

Y is a geometric factor for which the values of 1.13 and 1.3 were taken respectively for volume and surface defects [59].
The defect corresponding to the maximal stress intensity factor was retained as the critical defect in the sample.

The type, the size and the frequency of the retained critical defects are compared for U and H architectures in Table 2. As the samples were chamfered, potential critical defects were rarely detected at the edges; this was the case only for 4 H samples that presented large delamination defects on the tensile side. For this architecture, 85 % of the potential critical defects were detected on the tensile surface (including edge ones), and most of them could be considered as handling defects due to their large size (up to 84 µm). For U samples, surface defects are very small compared to those observed in H ones, and agglomerates near the tensile surface and perpendicular to the stress direction, were identified as the most critical defects in all samples. It is to not that agglomerates are also present in H samples. However, they are not fracture-initiation relevant for this architecture since they are parallel to the direction of tensile stress. Pores were rarely identified as potential critical defects (only in 15 % of H samples), in accordance with the small tensile stressed area in the used 3 points bending configuration, as it was also reported for ball on three balls tests in [20]. Moreover, their size is smaller than that of agglomerates in U samples.

3.3.2. Correlation with strength measurements

For the scanned samples, an effective strength, σ_{eff}, corresponding to the location (z_{CT}) of the XCT derived potential critical defect, was calculated from the measured strength, σ_f ($\sigma_{eff} = \sigma_f (1\text{-}z_{CT}/10)$). An XCT derived strength, $\sigma_{CT\text{-}f}$ was also determined using the Griffith criterion [60]:

$$\sigma_{CT-f} = \frac{K_{IC}}{Y\sqrt{a_{CT}}} \qquad (2)$$

where a_{CT} is the XCT derived defect size, K_{IC} is the fracture toughness taken as 4.9 $MPam^{1/2}$

(after [20]) and Y the geometrical factor used for eq. 1.

In Fig. 9, $\sigma_{CT\text{-}f}$ is plotted versus σ_{eff} for the critical defects retained in both U and H samples. A good agreement between the two values is obtained for almost all samples with greater consistency for U architecture. Indeed, in this case, the failure origins are agglomerates, similar to circular internal defects perpendicular to the applied stress, for which the geometrical factor used in the calculations for volume defects is particularly useful. For H architecture, large differences (> 100 MPa) were observed between $\sigma_{CT\text{-}f}$ and σ_{eff} for some samples and can be attributed essentially to the approximated values of the geometrical factors, as they are not precisely known for the large surface defects with complex shapes detected in XCT projection images. Moreover, the large delamination's observed in these samples could reduce the cross sections of the bars over a long distance and thus, may lead to underestimation of the experimental determined strengths (σ_{eff}). Precise calculations taking into account real defect shapes would reduce the differences between the XCT derived and the experimental effective strengths.

3.3.3. Correlation with SEM analysis

After the bending tests, a fractographic analysis using SEM was carried out on representative samples to verify the fracture origins. In most cases, the lasts are similarly positioned as predicted by XCT analysis and a very good agreement was found between XCT images and SEM micrographs of the fracture origins in H and U samples (Fig. 10 and 11). These results, added to the good correlation between XCT data with mechanical strength, clearly demonstrate that XCT analysis is entirely relevant to characterize the defects in AM dense ceramics in order to monitor and then to optimize their manufacturing process.

4. Conclusion

X-Ray computed tomography analysis was successfully applied for non-destructive detection of typical defects in LCM processed 3Y-TZP zirconia and allowed to obtain information on their 3D nature and distribution. Moreover, XCT analysis allowed the identification of potential critical defects with a good correlation with bending strength measurements and SEM observations of the fractured surfaces. Such advanced quantification of defects may be a powerful tool to qualify ceramics processed by AM and highlight the most critical defect populations, in order to improve process and reach very high-performance products.
References

[1] N. Travitzky, A. Bonet, B. Dermeik, T. Fey, I.F. Demut, L. Schlier, T. Schlordt and P. Greil, Additive Manufacturing of Ceramic-Based Materials, Adv. Eng. Mat. 16 (2014) 729-754. 10.1002/adem.201400097.

[2] A. Zocca, P. Colombo, C.M. Gomes, J. Gunster, Additive Manufacturing of Ceramics: Issues, Potentialities, and Opportunities, J. Am. Ceram. Soc. 98 (2015) 1983–2001. 10.1111/jace.13700.

[3] J. Ebert, E. Özkol, A. Zeichner, K. Uibel, Ö. Weiss, U. Koops, R. Telle and H. Fischer, Direct Inkjet Printing of Dental Prostheses Made of Zirconia, J. Dent. Res. 88 (2009) 673 – 676. 10.1177/0022034509339988.

[4] W.Y.Yeong, C.Y.Yap, M. Mapar & C.K. Chua, State-of-the-art review on selective laser melting of ceramics (2014), High value manufacturing : advanced research in virtual and rapid prototyping : proceedings of the 6th International Conference on Advanced Research and Rapid Prototyping, Leiria, Portugal, 1-5 October, 2013.

[5] Ph. Bertrand, F. Bayle, C. Combe, P. Goeuriot, I. Smurov, Ceramic components manufacturing by selective laser sintering, Appl. Surf. Sci. 254 (2007) 989 – 992. https://doi.org/10.1016/j.apsusc.2007.08.085.

[6] K. Shahzad, J. Deckers, Z. Zhang, J.P. Kruth, J, Vleugels, Additive manufacturing of zirconia parts by indirect selective laser sintering, J. Eur. Ceram. Soc. 34 (2014) 81–89. http://dx.doi.org/10.1016/j.jeurceramsoc.2013.07.023.

[7] J.W. Halloran, Ceramic Stereolithography: Additive Manufacturing for Ceramics by Photopolymerization, Annu. Rev. Mat. Res. 46 (2016) 19 – 40. 10.1146/annurev-matsci-070115-031841.

[8] M. Schwentenwein and J. Homa, Additive Manufacturing of Dense Alumina Ceramics, Int. J. Appl. Ceram. Technol. 12 (2014) 1–7. 10.1111/ijac.12319.

[9] W. Li, A. Ghazanfari, D. McMillen, M.C. Leu, G.E. Hilmas, J. Watts, Characterization of zirconia specimens fabricated by ceramic on-demand Extrusion, Ceram. Int. 44 (2018) 12245–12252. https://doi.org/10.1016/j.ceramint.2018.04.008.

[10] E. Feilden, E.G.T. Blanca, F. Giuliani, E. Saiz, L. Vandeperre, Robocasting of structural ceramic parts with hydrogel inks, J. Eur. Ceram. Soc. 36 (2016) 2525-2533. http://dx.doi.org/10.1016/j.jeurceramsoc.2016.03.001.

[11] Y. Uçar, I.A. Meric, O. Ekren, Layered Manufacturing of Dental Ceramics: Fracture Mechanics, Microstructure, and Elemental Composition of Lithography-Sintered Ceramic, J. Prosthodont. 28 (2018) 310-318. 10.1111/jopr.12748.

[12] W. Liu, H. Wu, M. Zhou, R. He, Q. Jiang, Z. Wu , Y. Cheng, X. Song, Y. Chen, S. Wu, Fabrication of fine-grained alumina ceramics by a novel process integrating

stereolithography and liquid precursor infiltration processing, Ceram. Int. 42 (2016) 17736 – 17741. http://dx.doi.org/10.1016/j.ceramint.2016.08.099.

[13] Z. Xing, W. Liu,Y. Chen, W. Li, Effect of plasticizer on the fabrication and properties of alumina ceramic by stereolithography based additive manufacturing, Ceram. Int. 44 (2018) 19939-19944. https://doi.org/10.1016/j.ceramint.2018.07.259.

[14] H.H. Tang, M.L. Chiu, H.C. Yen, Slurry-based selective laser sintering of polymer-coated ceramic powders to fabricate high strength alumina parts, J. Eur. Ceram. Soc. 31 (2011) 1383–1388. 10.1016/j.jeurceramsoc.2011.02.020.

[15] M. Michálek, M. Michálková, G. Blugan, J. Kuebler, Strength of pure alumina ceramics above 1 GPa, Ceram. Int. 44 (2018) 3255–3260. https://doi.org/10.1016/j.ceramint.2017.11.098.

[16] D. Casellas, M.M. Nagl, L. Llanes, M. Anglada, Fracture toughness of alumina and ZTA ceramics: microstructural coarsening effects, J. Mat. Pro. Tec. 143 (2003) 148–152. 10.1016/S0924-0136(03)00396-0.

[17] E. Ferraris, J. Vleugels, Y. Guo, D. Bourell, J.P. Kruth, B. Lauwers, Shaping of engineering ceramics by electro, chemical and physical processes, CIRP Annals. 65 (2016) 761–784. http://dx.doi.org/10.1016/j.cirp.2016.06.001.

[18] Y. Han, S. Li, T. Zhu, W. Wu, D. An, Z. Xie, Enhanced properties of pure alumina ceramics by oscillatory pressure sintering, Ceram. Int. 44 (2018) 5238–5241. https://doi.org/10.1016/j.ceramint.2017.12.133.

[19] E. Özkol, A.M. Wätjen, R. Bermejo, M. Deluca, J. Ebert, R. Danzer, R. Telle, Mechanical characterisation of miniaturised direct inkjet printed 3Y-TZP specimens for microelectronic applications, J. Eur. Ceram. Soc. 30 (2010) 3145–3152. 10.1016/j.jeurceramsoc.2010.07.016.

[20] W. Harrer, M. Schwentenwein, T. Lube, R. Danzer, Fractography of zirconia-specimens made using additive manufacturing (LCM) technology, J. Eur. Ceram. Soc. 37 (2017) 4331-4338. http://dx.doi.org/10.1016/j.jeurceramsoc.2017.03.018.

[21] B. Al-Amleh, K. Lyons, M. Swain, Clinical trials in zirconia: a systematic review, J. Oral. Rehabil. 37 (2010) 641– 652. 10.1111/j.1365-2842.2010.02094.x.

[22] I. Touaiher, M. Saadaoui, J. Chevalier, L. Preiss, H. Reveron, Fracture behavior of Ce TZP/Alumina/Aluminate composites with different amounts of transformation toughening. Influence of the testing methods, J. Eur. Ceram. Soc. 38 (2017) 1778-1789. https://doi.org/10.1016/j.jeurceramsoc.2017.09.052.

[23] M. Turon-Vinas, M. Anglada, Fracture toughness of zirconia from a shallow notch produced by ultra-short pulsed laser ablation, J. Eur. Ceram. Soc. 34 (2014) 3865–3870. http://dx.doi.org/10.1016/j.jeurceramsoc.2014.05.009.

[24] H. Wu, W. Liu, R. He, Z. Wu, Q. Jiang, X. Song, Y. Chen, L. Cheng, S. Wu, Fabrication of dense zirconia-toughened alumina ceramics through a stereolithography-based additive manufacturing, Ceram. Int. 43 (2017) 968-972. http://dx.doi.org/10.1016/j.ceramint.2016.10.027.

[25] J. Wilkes, Y.C. Hagedorn, W. Meiners and K. Wissenbach, Additive manufacturing of ZrO2-Al2O3 ceramic components by selective laser melting, Rapid. Prototyp. J. 19 (2013) 51– 57. 10.1108/13552541311292736.

[26] M.C.C.S.B. Moraes, C.N. Elias, J.D. Filho, L.G. de Oliveira, Mechanical Properties of Alumina-Zirconia Composites for Ceramic Abutments, Mat. Res. 7 (2004) 643-649. http://dx.doi.org/10.1590/S1516-14392004000400021.

[27] T. Zhu, Z. Xie, Y. Han, S. Li, Microstructure and mechanical properties of ZTA composites fabricated by oscillatory pressure sintering, Ceram. Int. 44 (2017) 505-510. http://dx.doi.org/10.1016/j.ceramint.2017.09.204.

[28] Y.C. Hagedorn, J. Wilkes, W. Meiners, K. Wissenbach, R. Poprawe, Net Shaped High Performance Oxide Ceramic Parts by Selective Laser Melting, Ph. Pro. 5 (2010) 587 – 594. 10.1016/j.phpro.2010.08.086.

[29] M. Zhou, W. Liu, H. Wu, X. Song, Y. Chen, L. Cheng, F. He, S. Chen, S.Wu, Preparation of a defect-free alumina cutting tool via additive manufacturing based on stereolithography – Optimization of the drying and debinding processes, Ceram. Int. 42 (2016) 11598-11602. http://dx.doi.org/10.1016/j.ceramint.2016.04.050.

[30] M.X. Gan, C.H. Wong, Experimental studies on the properties of selectively laser melted alumina spodumene Composite, Ceram. Int. 44 (2018) 19008 – 19015. https://doi.org/10.1016/j.ceramint.2018.07.144.

[31] E. Maire and P. J. Withers, Quantitative X-ray tomography, Int. Mat. Rev. 59 (2014) 1-43. 10.1179/1743280413Y.0000000023.

[32] Í.B. da Silva, X-ray Computed Microtomography technique applied for cementitious materials: A review, Micron. 107 (2018) 1–8. https://doi.org/10.1016/j.micron.2018.01.006.

[33] J.M. Hundley, Z.C. Eckel, E. Schueller, K. Cante, S.M. Biesboer, B.D. Yahata, T.A. Schaedler, Geometric characterization of additively manufactured polymer derived ceramics, Add. Ma. 18 (2017) 95 –102. http://dx.doi.org/10.1016/j.addma.2017.08.009.

[34] I. Maskery, N.T. Aboulkhair, M.R. Corfield, C. Tuck, A.T. Clare, R.K. Leach, R.D.Wildman, I.A. Ashcroft, R.J.M. Hague, Quantification and characterisation of porosity in selectively laser melted Al–Si10–Mg using X-ray computed tomography, Mat. Char. 111 (2016) 193–204. http://dx.doi.org/10.1016/j.matchar.2015.12.001.

[35] B. Gapinski, P. Janicki, L.M. Podsadna, M. Jakubowicz, Application of the computed tomography to control parts made on additive manufacturing process, Pro. Eng. 149 (2016) 105 – 121. 10.1016/j.proeng.2016.06.645.

[36] F.H. Kim, S.P. Moylana, E.J. Garboczi, J.A. Slotwinski, Investigation of pore structure in cobalt chrome additively manufactured parts using X-ray computed tomography and three-dimensional image analysis, Add. Ma. 17 (2017) 23 – 38. http://dx.doi.org/10.1016/j.addma.2017.06.011.

[37] P. Shah, R. Racasan, P. Bills, Comparison of different additive manufacturing methods using computed tomography, Case. Stud. Nondestr. Test. Eval. 6 (2016) 69–78. http://dx.doi.org/10.1016/j.csndt.2016.05.008.

[38] A. Morales Rodriguez, P. Reynaud, G. Fantozzi, J. Adrien and E. Maire, Porosity analysis of long-fiber-reinforced ceramic matrix composites using X-ray tomography, Scripta. Mat. 60 (2009) 388 – 390. 10.1016/j.scriptamat.2008.11.018.

[39] H. Bale, M. Blacklock, M.R. Begley, D.B. Marshall, B.N. Cox and R.O. Ritchie, Characterizing Three-Dimensional Textile Ceramic Composites Using Synchrotron X-Ray Micro-Computed-Tomography, J. Am. Ceram. Soc. 95 (2012) 392 – 402. 10.1111/j.1551-2916.2011.04802.x.

[40] Y. Gao,Y. Wang, X. Yang, M. Liu, H. Xia, P. Huai, X. Zhou, Synchrotron X-ray tomographic characterization of CVI engineered 2D-wovenand 3D-braided SiCf/SiC composites, Ceram. Int. 42 (2016) 17137-17147. http://dx.doi.org/10.1016/j.ceramint.2016.08.001.

[41] L. Saucedo-Mora, T. Lowe, S. Zhao, P.D. Lee, P.M. Mummery, T.J. Marrow, In situ observation of mechanical damage within a SiC-SiC ceramic matrix composite, J. Nuc. Mat. 481 (2016) 13-23. http://dx.doi.org/10.1016/j.jnucmat.2016.09.007.

[42] F. Wan, S. Zhao, R. Liu, C. Zhang and T.J. Marrow, In situ Observation of Compression Damage in a Three-Dimensional Braided Carbon Fiber Reinforced Carbon and Silicon Carbide (C/C-SiC) Ceramic Composite, Microsc. Microanal. 24 (2018) 227-237. 10.1017/S1431927618000351.

[43] N.M. Larson, F.W. Zok, In-situ 3D visualization of composite microstructure during polymer-to-ceramic conversion, Acta. Mat. 144 (2018) 579 – 589. https://doi.org/10.1016/j.actamat.2017.10.054.

[44] E. Maire, P. Colombo, J. Adrien, L. Babout, L. Biasetto, Characterization of the morphology of cellular ceramics by 3D image processing of X-ray tomography, J. Eur. Ceram. Soc. 27 (2007) 1973–1981. 10.1016/j.jeurceramsoc.2006.05.097.

[45] L. Andersson, A.C. Jones, M.A. Knackstedt, L. Bergström, Three-dimensional structure analysis by X-ray micro-computed tomography of macroporous alumina templated with expandable microspheres, J. Eur. Ceram. Soc. 30 (2010) 2547 – 2554. 10.1016/j.jeurceramsoc.2010.05.003.

[46] N.O. Shanti, V.W.L. Chan, S.R. Stock, F. De Carlo, K. Thornton, K.T. Faber, X-ray micro-computed tomography and tortuosity calculations of percolating pore networks, Acta. Mat. 71 (2014) 126–135. http://dx.doi.org/10.1016/j.actamat.2014.03.003.

[47] S.M. Miller, X. Xiao, K.T. Faber, Freeze-cast alumina pore networks: Effects of freezing conditions and dispersion medium, J. Eur. Ceram. Soc. 35 (2015) 3595–3605. http://dx.doi.org/10.1016/j.jeurceramsoc.2015.05.012.

[48] A.M. Stanciuc, C.M. Sprecher, J. Adrien, L.I. Roiban, M. Alini, L. Gremillard, M. Peroglio, Robocast zirconia-toughened alumina scaffolds: Processing, structural characterisation and interaction with human primary osteoblasts, J. Eur. Ceram. Soc. 38 (2018) 845–853. http://dx.doi.org/10.1016/j.jeurceramsoc.2017.08.031.

[49] M. Ahlhelm, D. Werner, J. Maier, J. Abel, T. Behnisch, T. Moritz, A. Michaelis, M. Gude, Evaluation of the pore morphology formation of the Freeze Foaming process by in situ computed tomography, J. Eur. Ceram. Soc. 38 (2018) 3369 - 3378. https://doi.org/10.1016/j.jeurceramsoc.2018.02.031.

[50] K. Moritz, T. Moritz, ZrO2 ceramics with aligned pore structure by EPD and their characterisation by X-ray computed tomography, J. Eur. Ceram. Soc. 30 (2010) 1203–1209. 10.1016/j.jeurceramsoc.2009.05.034.

[51] S. Cottrino, Y. Jorand, E. Maire, J. Adrien, Characterization by X-ray tomography of granulated alumina powder during in situ die compaction, Mat. Char. 81 (2013) 111 – 123. http://dx.doi.org/10.1016/j.matchar.2013.04.004.

[52] D. Bernard, D. Gendron, J.M. Heintz, S. Bordere, J. Etourneau, First direct 3D visualisation of microstructural evolutions during sintering through X-ray computed microtomography, Acta. Mat. 53 (2005) 121–128. 10.1016/j.actamat.2004.09.027.

[53] S. Renold Elsen,T. Ramesh, Shrinkage characteristics studies on conventional sintered zirconia toughened alumina using computed tomography imaging technique, Int. J. Refract. Met. Hard. Mat. 54 (2016) 383–394. http://dx.doi.org/10.1016/j.ijrmhm.2015.09.008.

[54] T. Hondo, Z. Kato, K. Yasuda, F. Wakai, S. Tanaka, Coarse pore evolution in dry-pressed alumina ceramics during sintering, Adv. Powder. Tec. 27 (2016) 1006 – 1012. http://dx.doi.org/10.1016/j.apt.2016.04.009.

[55] Y. Vertyagina, M. Mostafavi, C. Reinhard, R. Atwoodc, T.J. Marrow, In situ quantitative three-dimensional characterisation of sub-indentationcracking in polycrystalline alumina, J. Eur. Ceram. Soc. 34 (2014) 3127–3132. http://dx.doi.org/10.1016/j.jeurceramsoc.2014.04.002.

[56] G. Pećanac, J. Malzbender, F. Pauly, M.L. Fontaine, P. Niehoff, S. Baumann, T. Beck, L. Singheiser, Mechanical characterization of ceramics by means of a 3D defect analysis, Ceram. Int. 41 (2015) 2411–2417. http://dx.doi.org/10.1016/j.ceramint.2014.10.055.

[57] J. Chevalier, C. Olagnon, G. Fantozzi, Crack propagation and fatigue in zirconia-based composites, Compos Part A. Appl. Sci. Manuf. 30 (1999) 525-530. https://doi.org/10.1016/S1359-835X(98)00145-6.

[58] I.J. Davies, Confidence limits for Weibull parameters estimated using linear leastsquares analysis, J. Eur. Ceram. Soc. 37 (2017) 5057-5064. http://dx.doi.org/10.1016/j.jeurceramsoc.2017.05.051.

[59] G. D. Quinn, Fractography of Ceramics and Glasses, NIST Recommended Practice Guide, Special Publication 960-16; National Institute of Standards and Technology, Gaithersburg, US, 2007.

[60] D. Munz, T. Fett, Ceramics: Mechanical Properties, Failure Behavior, and Materials Selection, Springer Verlag, NewYork, 1999.

Figures

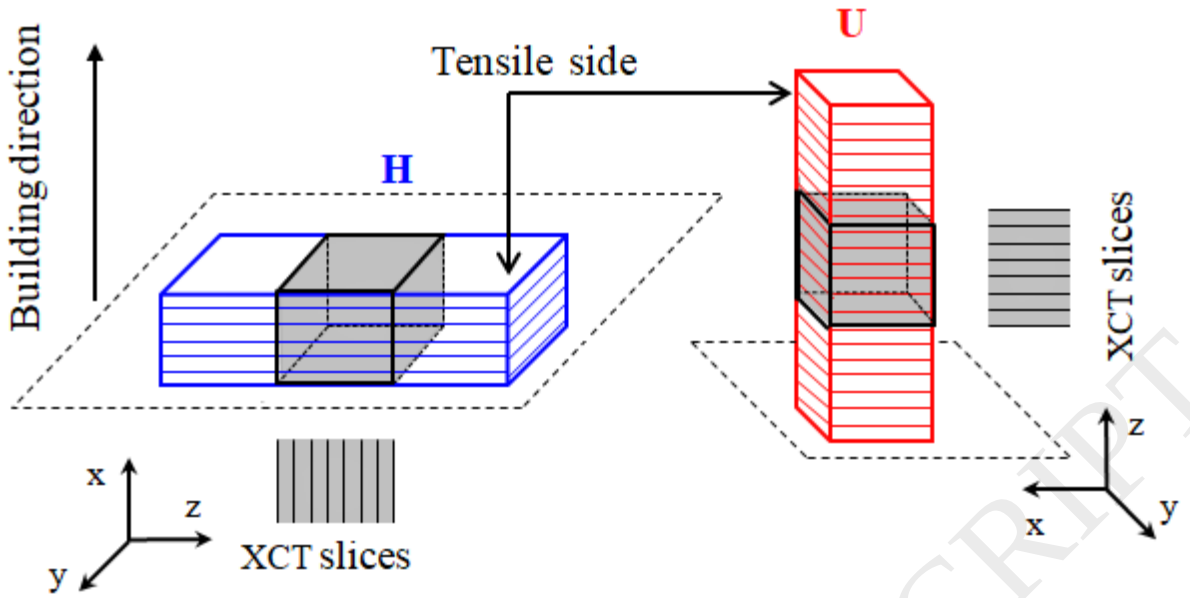

Fig. 1. Schematic representation of the horizontal (H) and upright (U) architectures showing the orientation of the material layers in relation to the tensile side and the direction, z, of XCT scans completed over a length of 10 mm at the center of the specimens (colored area).

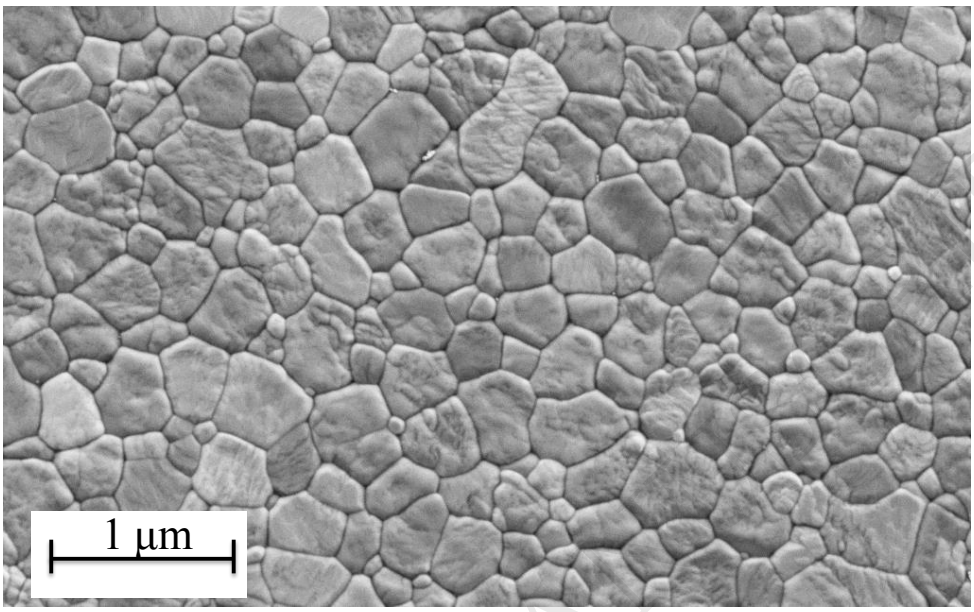

Fig. 2. SEM micrograph of 3Y-TZP studied material.

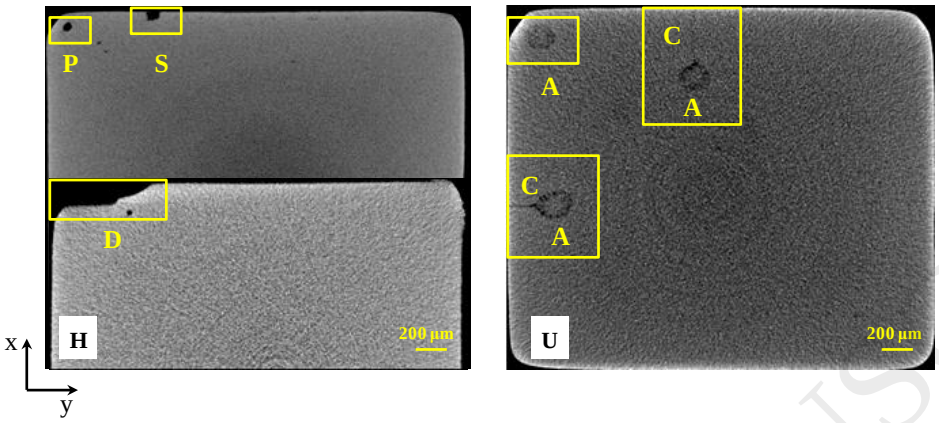

Fig. 3. Examples of XCT slices showing typical detected defects. Pores (P) are present in both H and U architectures, delamination (D) and large surface defects (S) were detected in H samples and agglomerates (A) with associated cracks (C) are typical of U samples.

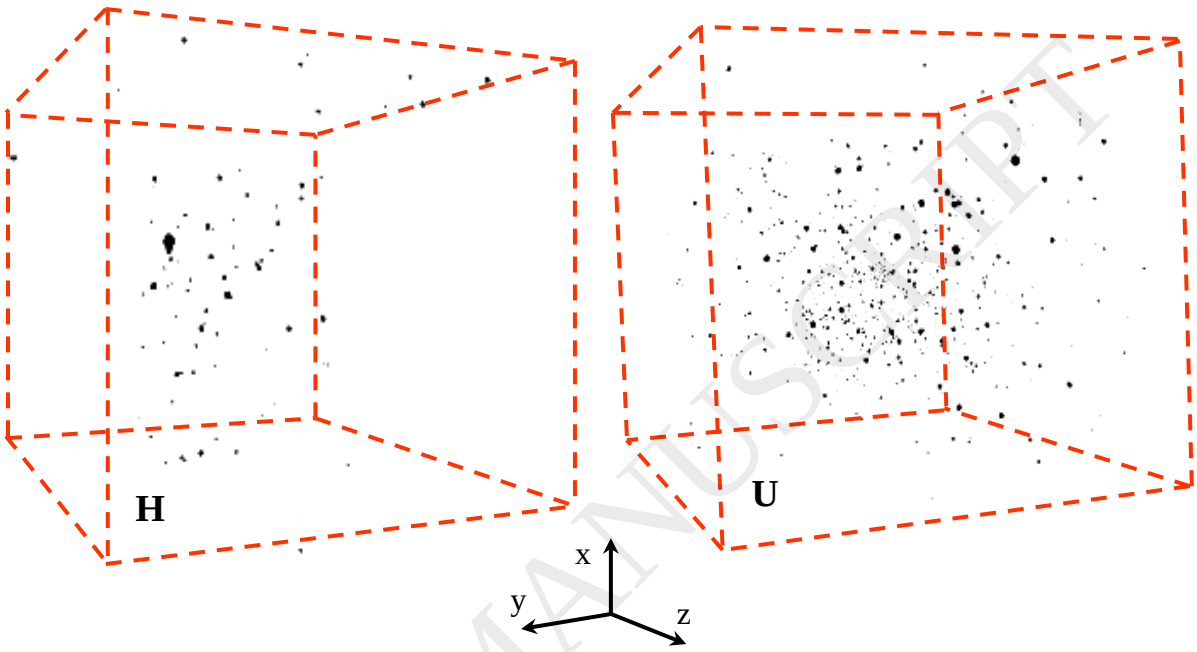

Fig. 4. 3D XCT reconstructions showing the pores distribution in H and U samples (Observation volume: 2.2 x 2.5 x 2.5 mm^3).

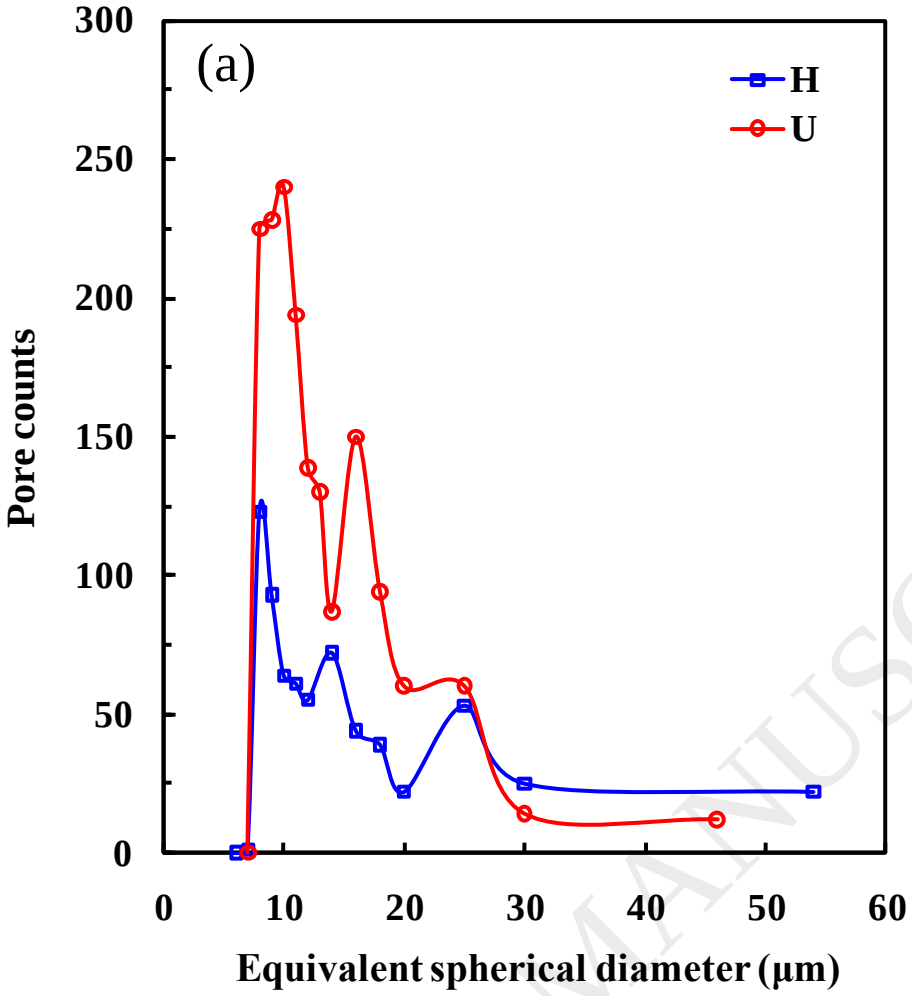

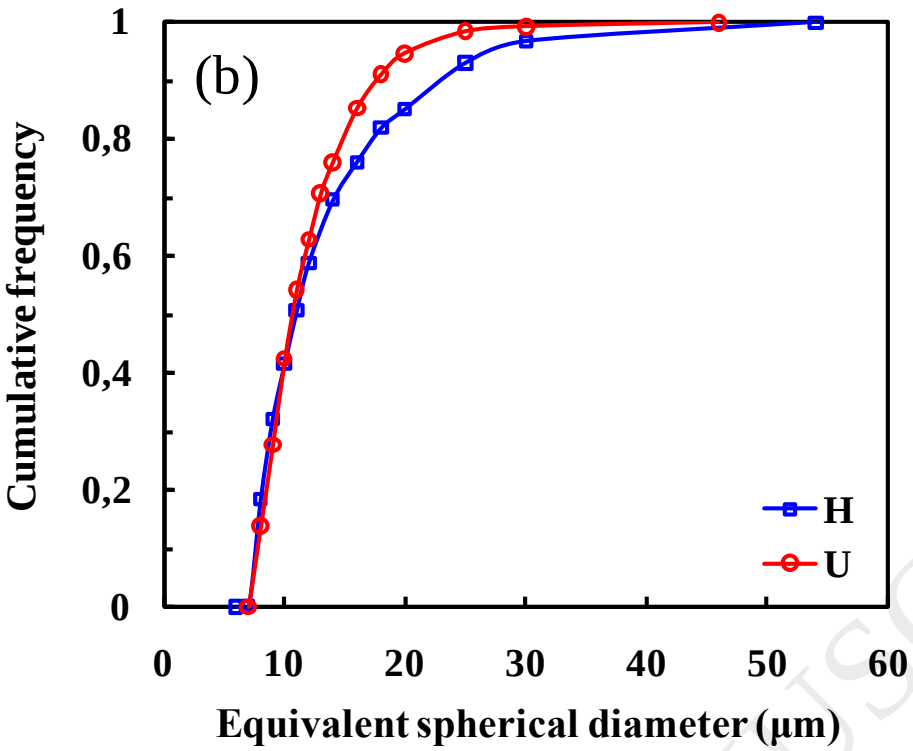

Fig. 5. Pore size distribution (a) and cumulative pore size distribution (b) in H and U samples, over the total scanned volume (2.2 x 2.5 x 10 mm^3).

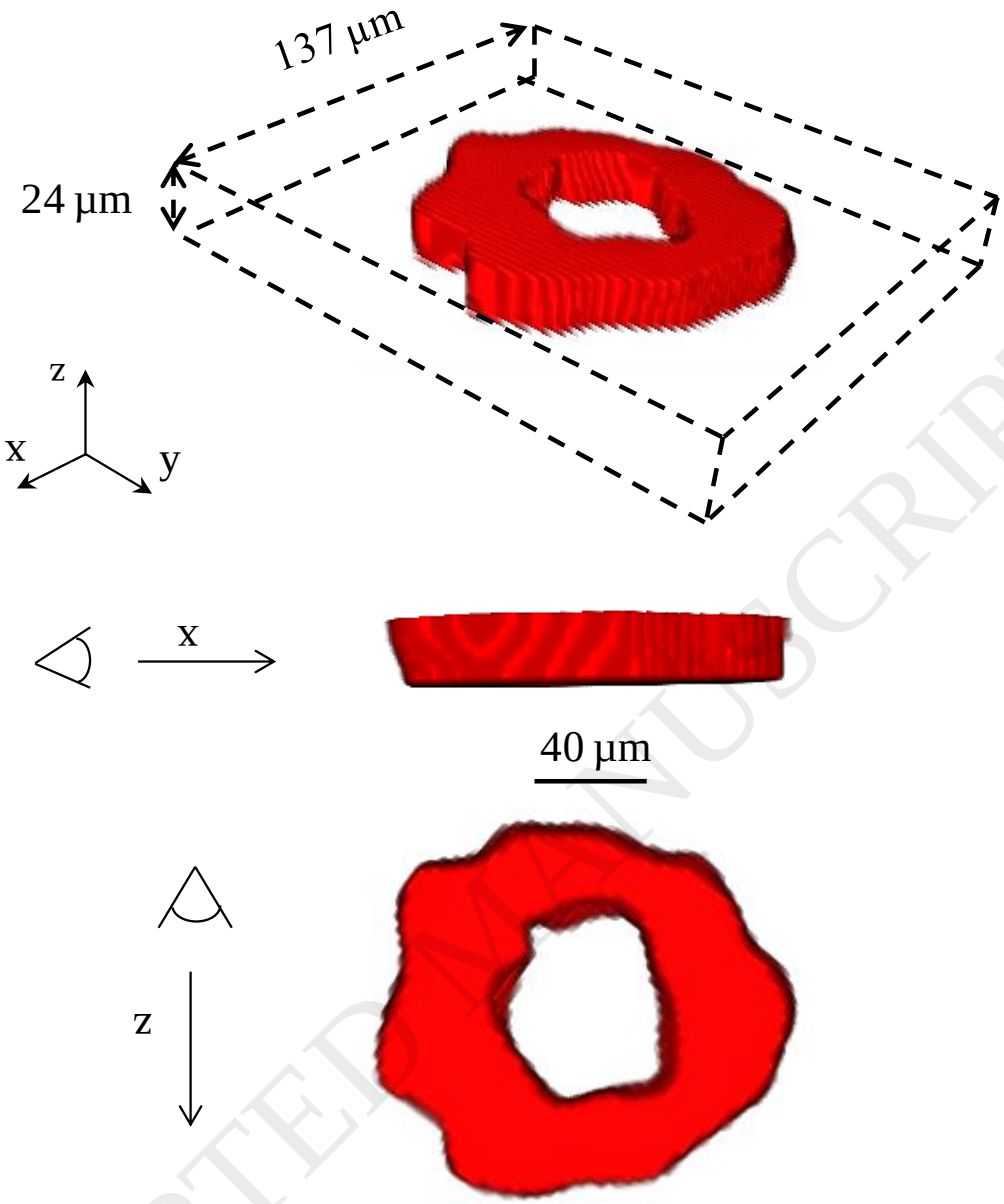

Fig. 6. Example of 3D perspective view of an agglomerate, with views in x and z directions. Colored area correspond to under-densified zones.

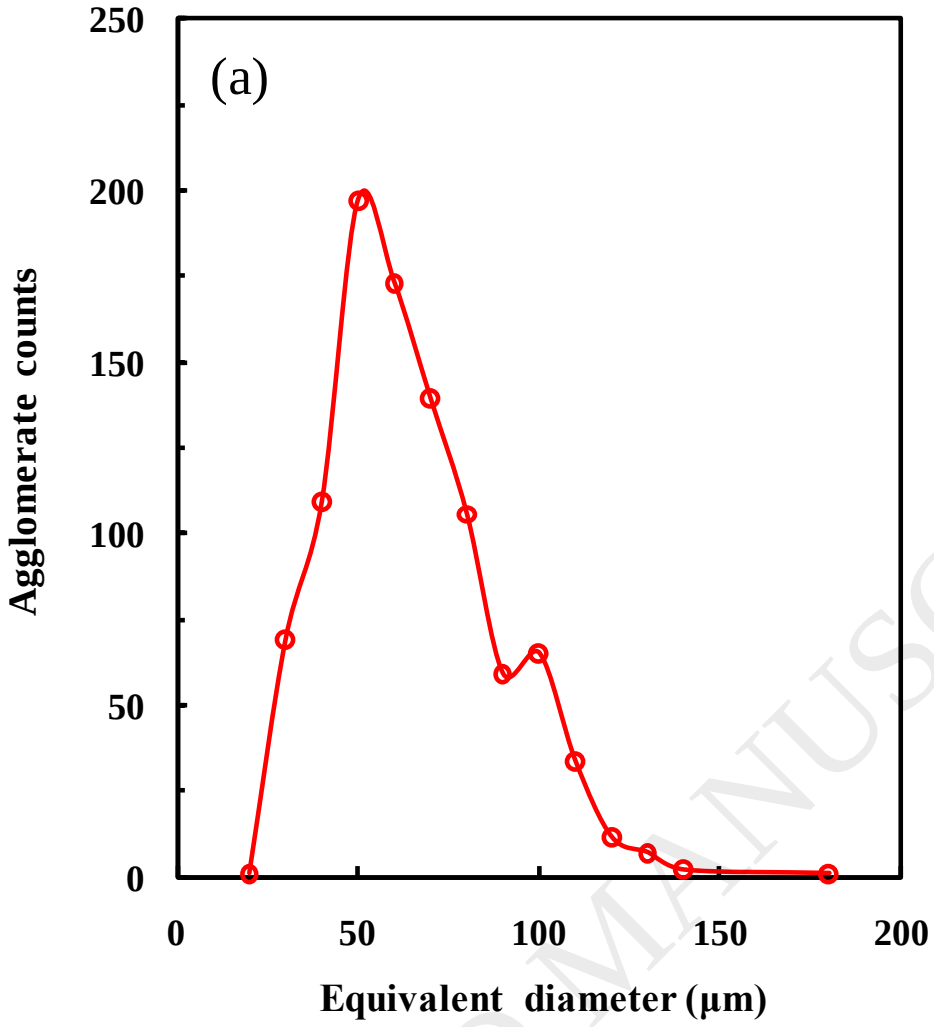

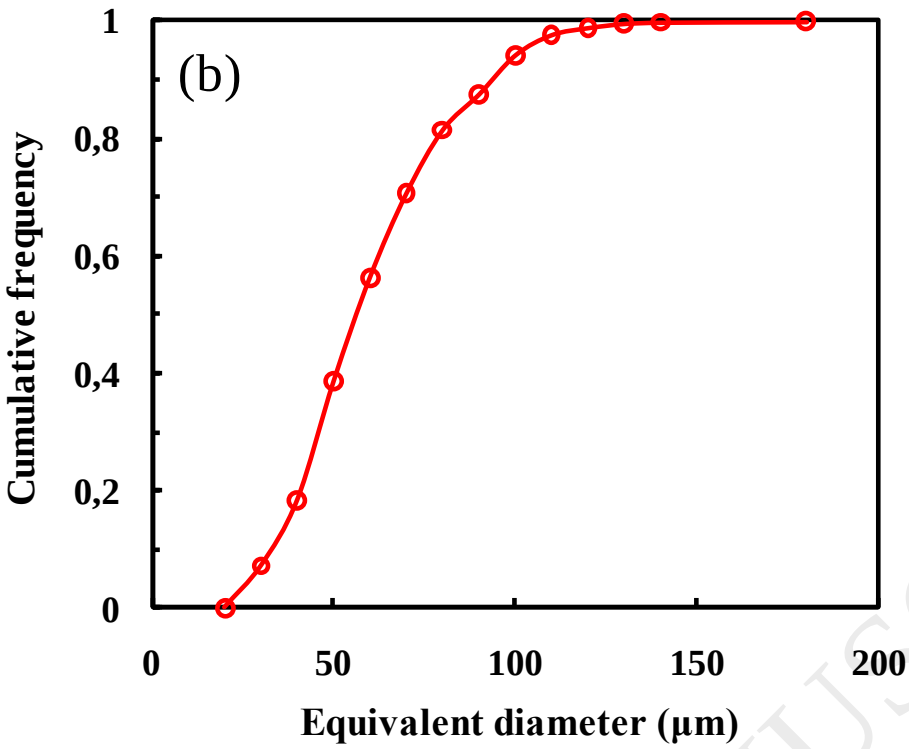

Fig. 7. Agglomerate size distribution (a) and cumulative agglomerate size distribution (b), over a total scanned volume (2.2 x 2.5 x 10 mm^3) of U sample.

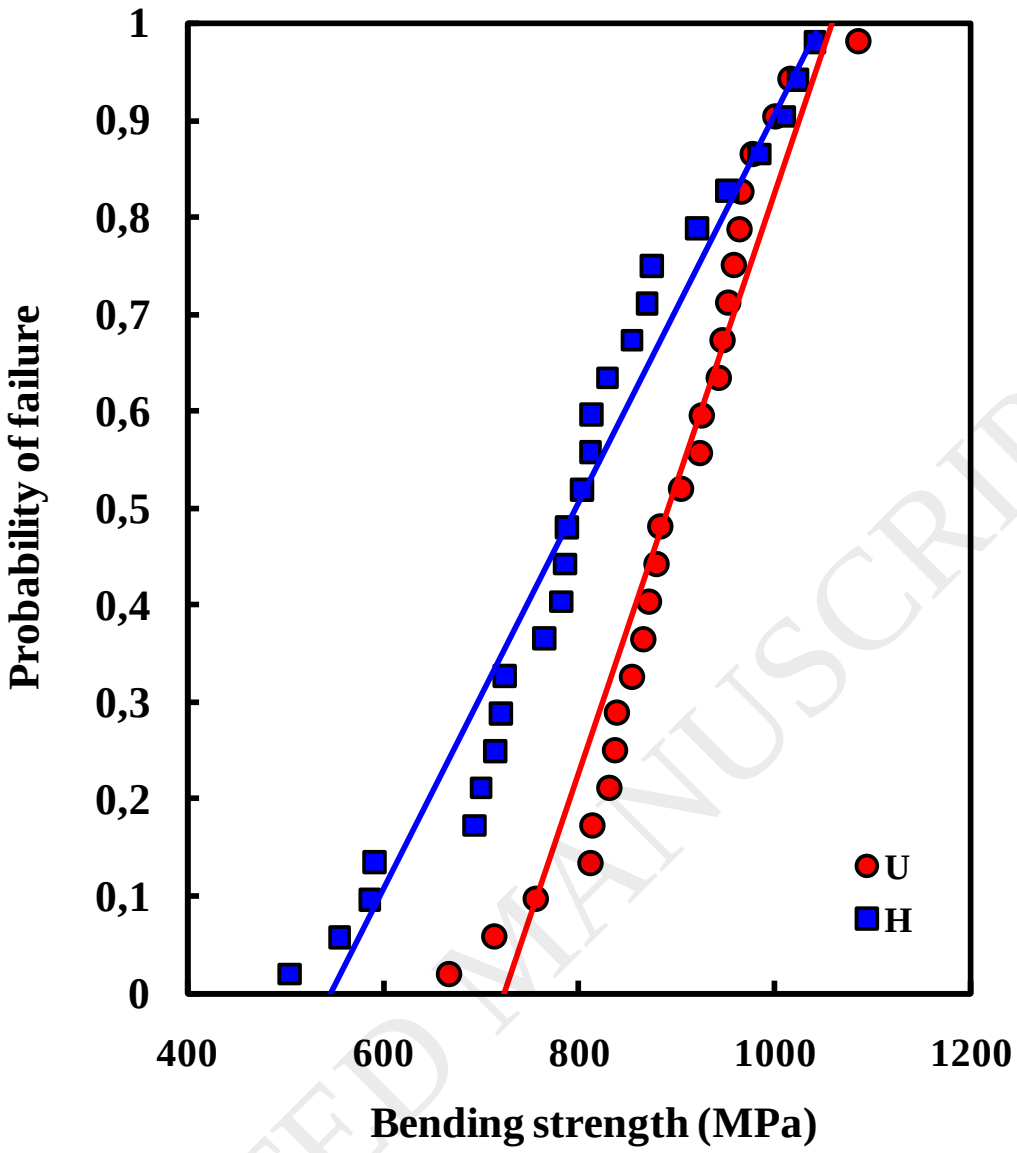

Fig. 8. Weibull plot showing the probability of failure versus strength.

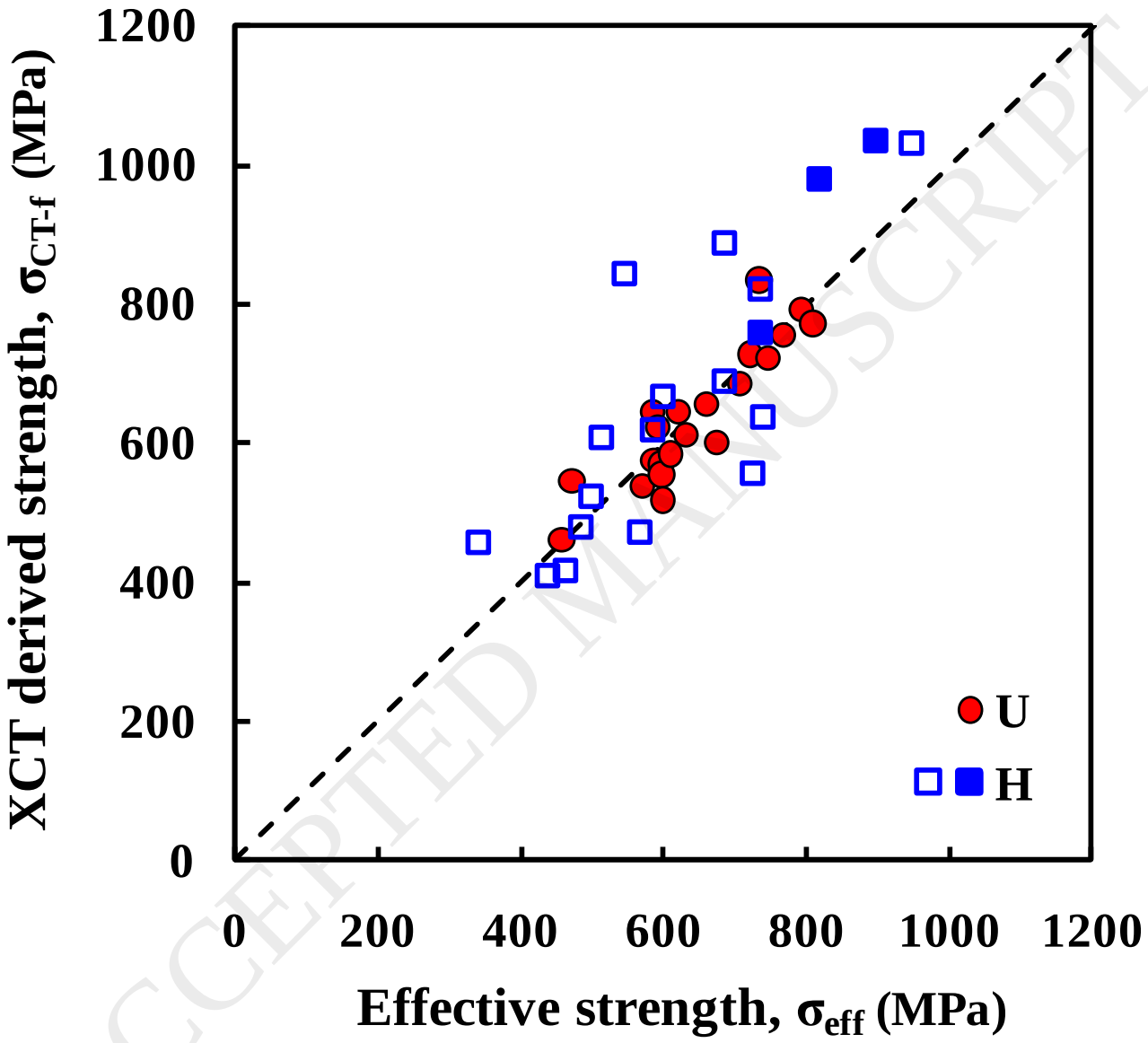

Fig. 9. Correlation between the effective and the XCT derived strengths. Open symbols correspond to surface defects and solid ones to volume defects (i.e. agglomerates for U samples and pores for H samples).

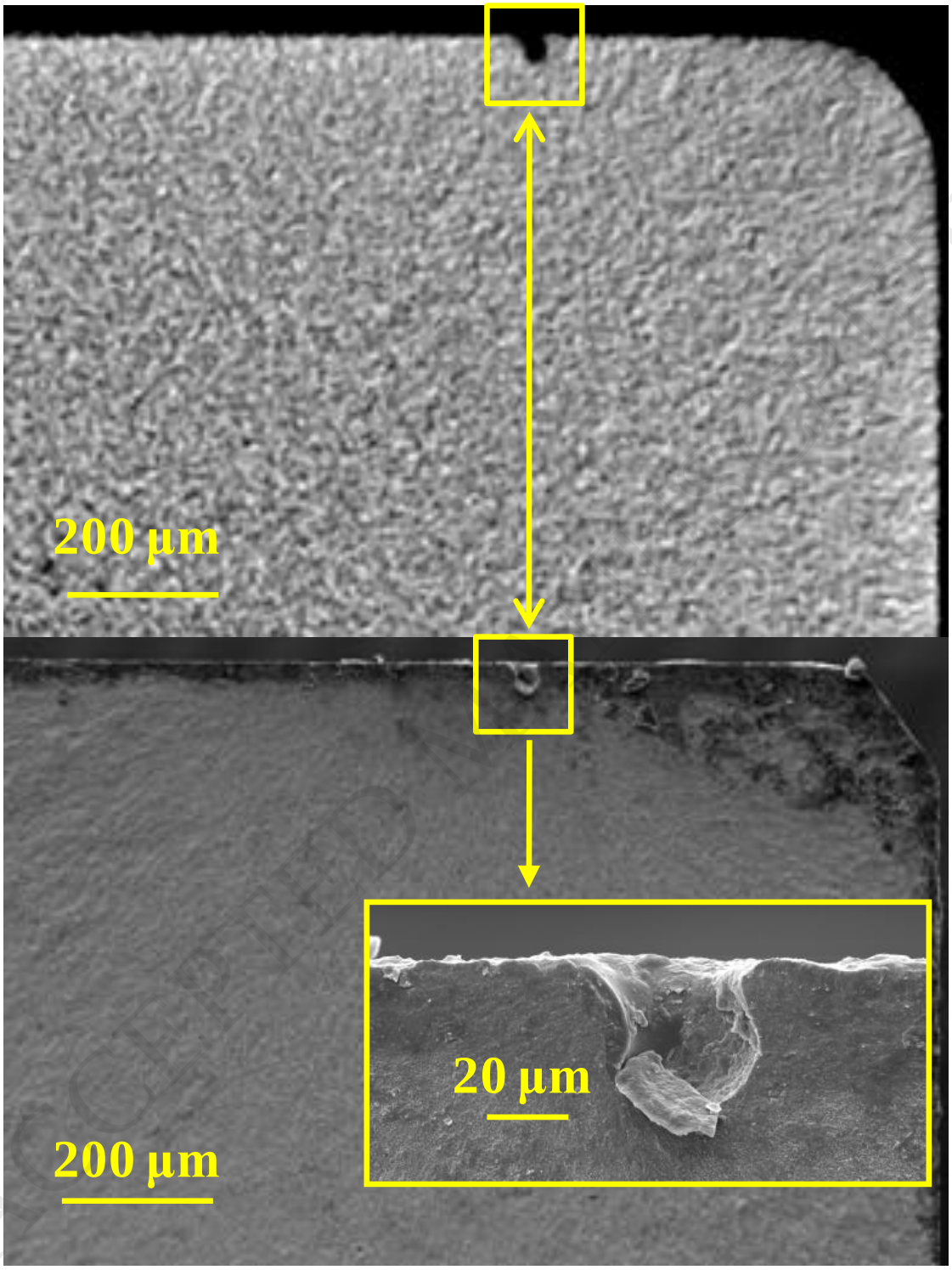

Fig. 10. Example of comparison between an XCT slice of H sample containing the potential surface critical defect (a), and corresponding SEM micrograph of the fracture surface (b). Upper surface corresponds to the tensile side.

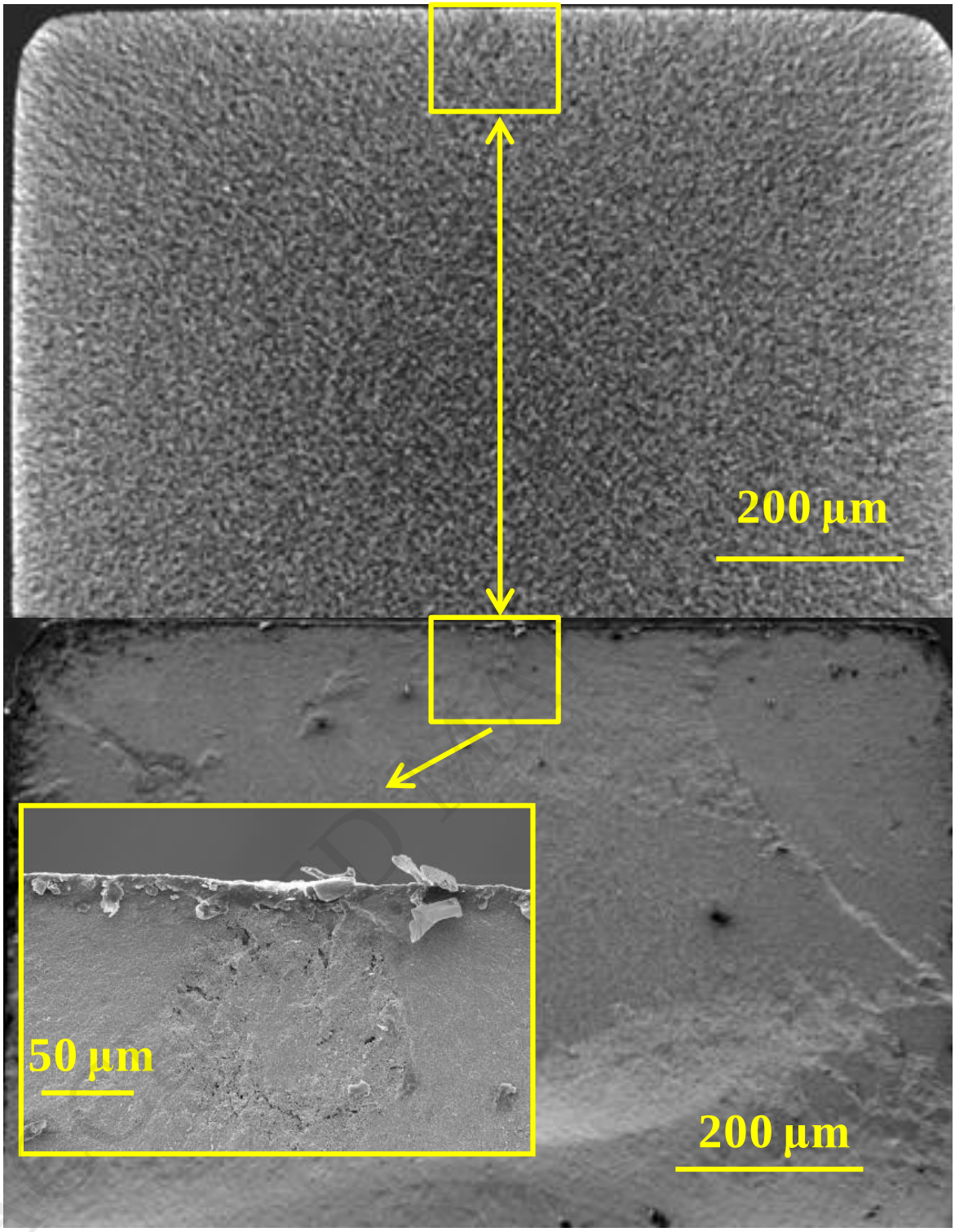

Fig. 11. Example of comparison between an XCT slice of U sample containing the potential agglomerate critical defect (a) and corresponding SEM micrograph of the fracture surface,

corroborating the presence of 150 μm-sized agglomerate (b). Upper surface corresponds to the tensile side.

Tables

Table 1: Properties of alumina, 3YTZP zirconia and zirconia toughened alumina (ZTA) processed by additive manufacturing (AM) compared to those obtained for conventional manufacturing (CM). Subscript symbols defined below indicate the testing methods for toughness and strength measurements.

Material	Process	Density (%)	Grain size (µm)	Vickers hardness (GPa)	Toughness (MPa.m$^{1/2}$)	Strength (MPa)	Weibull modulus	References
	AM							
	DIW	97	1.4	18.6	3.31 ^{IF}	230 ^{4P}	8.9	[10]
	LCM	99.3	3.05	-	-	427 ^{4P}	11.2	[8]
Al_2O_3	LCM	-	-	15.8	6.5 ^{FA}	490 ^{B3B}	11.43	[11]
	SLA	-	4.22	17.2	5.94 ^{IF}	-	-	[12]
	SLA	98.5	1.9	-	-	486 ^{3P}	-	[13]
	SLS	98	-	-	-	363.5 ^{3P}	-	[14]
	CM	> 99	2 – 4	17 -1 8	3 - 4	300-500	8-11	[15-18]
	AM							
	DIP	96.9	-	-	6.7 ^{SEVNB}	763 ^{4P}	3.5	[3]
3Y-TZP	DIP	-	< 1	-	-	1393 ^{B3B}	10.4	[19]
	CODE	99.1	0.81	13.1	4.6 ^{CNB}	563 ^{4P}	7.9	[9]
	LCM	99	-	13.4	4.9 ^{SEVNB}	878 ^{4P}	11.1	[20]
	CM	> 99	< 1	≈13	4 - 6 ^{SEVNB}	900- 1200	13-17	[19,21-23]
ZTA*	**AM**							
20	SLA	99.5	1.08	17.8	5.7 ^{IF}	530 ^{3P}	-	[24]
41.5	SLM	> 99	-	-	-	538 ^{B3B}	-	[25]
20-21	**CM**	> 99	< 1	17-19	5-7	500 -1000	13	[26, 27]

SEVNB: Single Edge V Notched Beam.
IF: Indentation Fracture method.
FA: Fractographic Analysis.
CNB: Chevron Notched Beam.
3P: three points bending test
4P: four points bending test.
B3B: biaxial ball-on-three balls test.
* indicated is the wt% of zirconia and the grain size of alumia.

Table 2: Fracture origins detected by XCT before 3P-bending tests (21 samples for each architecture).

Defects	Sample H		Sample U	
	Number	Size (µm)	Number	Size (µm)
Agglomerate	0	0	21	54 – 173
Surface	12	13 – 84	0	0
Edge	4	35 – 68	0	0
Pore	3	35 – 65	0	0
Not determined*	2	0	0	0

*Fractured out of the scanned area